ARL-TR-9959 • AUG 2024

Evaluation of Near-Eutectic Al–Mg–Zn Alloys

by Taylor W Cain and Jon-Erik Mogonye

ARL-TR-9959 ● AUG 2024

Evaluation of Near-Eutectic Al–Mg–Zn Alloys

Taylor W Cain and Jon-Erik Mogonye
DEVCOM Army Research Laboratory

REPORT DOCUMENTATION PAGE

1. REPORT DATE	2. REPORT TYPE	3. DATES COVERED START DATE	END DATE
August 2024	Technical Report	12 December 2021	7 July 2024

4. TITLE AND SUBTITLE
Evaluation of Near-Eutectic Al–Mg–Zn Alloys

5a. CONTRACT NUMBER	5b. GRANT NUMBER	5c. PROGRAM ELEMENT NUMBER
5d. PROJECT NUMBER	**5e. TASK NUMBER**	**5f. WORK UNIT NUMBER**

6. AUTHOR(S)
Taylor W Cain and Jon-Erik Mogonye

7. PERFORMING ORGANIZATION NAME(S) AND ADDRESS(ES)	8. PERFORMING ORGANIZATION REPORT NUMBER
DEVCOM Army Research Laboratory ATTN: FCDD-RLA-MF Aberdeen Proving Ground, MD 21005	ARL-TR-9959

9. SPONSORING/MONITORING AGENCY NAME(S) AND ADDRESS(ES)	10. SPONSOR/MONITOR'S ACRONYM(S)	11. SPONSOR/MONITOR'S REPORT NUMBER(S)

12. DISTRIBUTION/AVAILABILITY STATEMENT
DISTRIBUTION STATEMENT A. Approved for public release: distribution unlimited.

13. SUPPLEMENTARY NOTES

ORCID IDs: Taylor W Cain, 0000-0002-6621-914X; Jon-Erik Mogonye, 0000-0002-7508-083X

14. ABSTRACT

Near eutectic ternary Al–Mg–Zn alloys were cast and evaluated for their mechanical and thermal properties. The results revealed extremely high hardness for these alloys in comparison to traditional Al-based cast alloys due to a high volume fraction of the divorced eutectic τ-Mg32(Al,Zn)49 phase. However, negligible room temperature ductility was discovered for all alloys, which limits the prospects of these alloys for industrialization.

15. SUBJECT TERMS
aluminum casting, aluminum alloy, eutectic alloy, aluminum magnesium zinc alloy, T-phase, Mechanical Sciences, Sciences of Extreme Materials

16. SECURITY CLASSIFICATION OF: a. REPORT	b. ABSTRACT	C. THIS PAGE	17. LIMITATION OF ABSTRACT	18. NUMBER OF PAGES
UNCLASSIFIED	UNCLASSIFIED	UNCLASSIFIED	UU	28

19a. NAME OF RESPONSIBLE PERSON	19b. PHONE NUMBER *(Include area code)*
Taylor W Cain	(410) 278-3162

STANDARD FORM 298 (REV. 5/2020)
Prescribed by ANSI Std. Z39.18

Contents

List of Figures

List of Tables

Acknowledgments

We would like to thank Mr Christopher Carangelo (Booz Allen Hamilton), who completed the tensile testing for this report.

1. Introduction

The desire for increased fuel efficiency, range, and speed of aviation platforms led to increased demand for lightweight alloys that can maintain high performance over a range of temperature conditions. Recently, research on Al–Ce-based alloys has exploded due to their excellent creep resistance and retention of mechanical properties at temperatures up to 350 °C.[1–17] In contrast, there is a paucity of data on Al–Mg–Zn-based eutectic alloys in the literature. One study on Al–Mg–Zn eutectic alloys evaluated the effect of composition and solidification pathways on mechanical properties.[18] The alloy $Al_{54}Mg_{22.5}Zn_{23.5}$ (MZ2324) possessed excellent yield strength retention with increasing temperature compared to legacy cast Al alloys (Fig. 1). However, no ductility of this eutectic alloy is observed below 250 °C, which limits its potential for use in many applications.

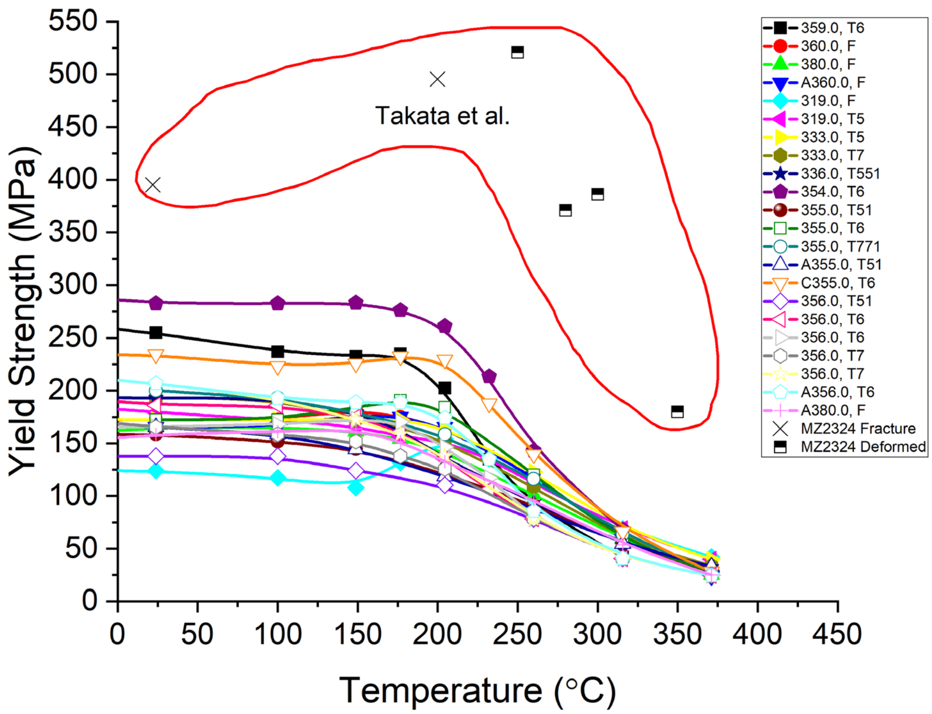

Fig. 1 Plot of yield strength vs. temperature for various cast Al alloys from the ASM handbook.[19] The data from Takata et al. represented by the crosses are fracture strengths while the half-filled squares have some ductility.[18]

The goal of this study is to evaluate if decreasing the fraction of eutectic microstructure could sufficiently increase low-temperature ductility for consideration in engine applications. To test this, two hypoeutectic Al–Mg–Zn alloys were cast while maintaining the same Mg:Zn ratio as the $Al_{54}Mg_{22.5}Zn_{23.5}$ in the work by Takata et al.[18] Compositions were first selected by surveying various thermodynamic properties using the Thermo-Calc software package. Alloys of the desired compositions were then cast and characterized via a suite of microscopic and X-ray methods followed by mechanical and thermal property evaluation.

2. Methods and Procedures

2.1 Melting and Casting of Alloys

All alloys in this investigation were prepared by melting and casting in an Indutherm VTC 800 V/Ti vacuum induction casting machine using 99.95% pure pellets of Al, Mg, and Zn. The targeted compositions in Table 1 were cast into a 35-mm-diameter × 80-mm-height graphite mold packed in sand at ambient temperature. Additional castings were produced in a Cu wedge mold preheated at 400 °C as discussed in Cain and Mogonye.[20] The alloy charge was allowed to melt under Ar atmosphere and were mechanically mixed every 5 min for 15 min prior to casting. All alloys were cast at +50 °C above their liquidus as calculated by Thermo-Calc with the TCAL5 database.

Table 1 Targeted composition of Al–Mg–Zn alloys

Alloy ID	At.%			Wt.%		
	Al	Mg	Zn	Al	Mg	Zn
MZ1617	67.7	15.8	16.5	55.5	11.7	32.8
MZ1920	60.9	19.1	20	48.1	13.6	38.3
MZ2324	54	22.5	23.5	41.2	15.4	43.4

2.2 Metallographic Preparation and Physical Characterization Methods

Samples were prepared for scanning electron microscopy (SEM) by grinding to a CAMI (Coated Abrasives Manufacturing Institute) 1200-grit finish using SiC grinding papers. Samples were further polished using water-based 1- and 0.25-µm diamond polishing solutions with a final polishing step in a water-based 0.05-µm Al_2O_3 suspension. SEM was performed using a Hitachi SU3500 scanning electron microscope in backscattered electron (BSE) mode at an accelerating voltage of 20 kV. Energy-dispersive X-ray spectroscopy (EDS) was performed using the Bruker QUANTAX EDS system. Additional microscopy was performed using a Keyence VK X-1000 laser microscope utilizing the optical imaging mode.

The crystalline structure of each alloy was determined using X-ray diffraction. In this study, a Bruker D2 Phaser equipped with Co X-ray source (K_α λ = 1.7902 Å) was used. Experiments were performed in the Bragg-Brentano geometry with a 2θ scan range of 15°–90°, step size of 0.02°, and dwell of 1 s per step.

2.3 Mechanical Property Determination

The mechanical properties of each alloy were first evaluated using micro-Vickers hardness. This was performed with a 1-kgf load with a 5-s load time, 10-s dwell time, and 5-s unload time on a Mitutoyo HM-200. Additional mechanical testing was performed on wedge castings using the test cut plan shown in Fig. 2. First, book-matched plates 2 mm in thickness were sectioned from the centerline of the wedge using wire electrical discharge machining (EDM). Modified subsize ASTM E8[21] dog bone style tensile bars (Fig. 3) were cut out of one plate while the other plate was held in reserve. In addition, cylinders were sectioned for coefficient of thermal expansion (CTE) determination. Quasi-static tensile testing was performed at room temperature using an Admet eXpert 2611 load frame.

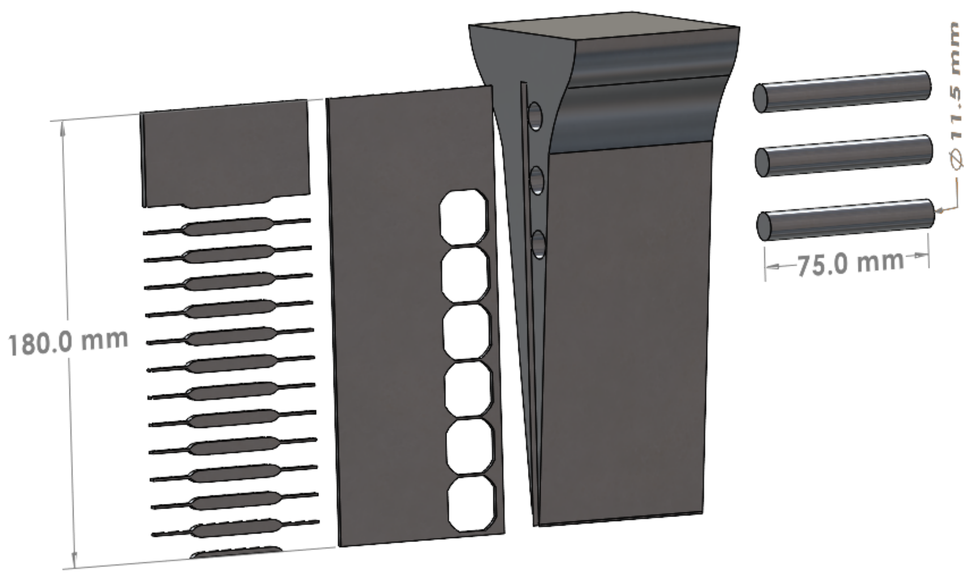

Fig. 2 Exploded view of samples sectioned from the wedge castings

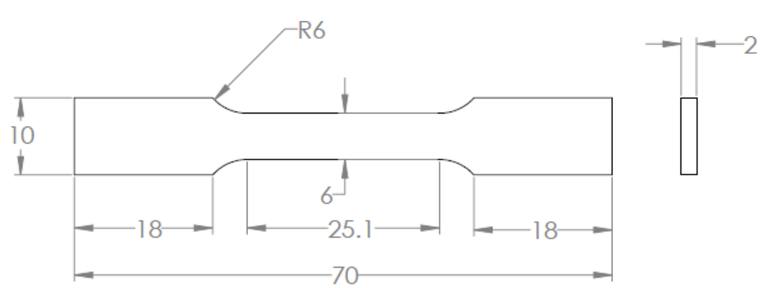

Fig. 3 Schematic for modified subsize ASTM E8 flat dog bone style tensile specimens. Dimensions are in millimeters.

2.4 Dilatometry

Dilatometry was performed on MZ1617 using an Orton 2016STD on samples 0.2 inch in diameter and 1 inch in length. The machine was first calibrated using 99.99% pure Cu rod of the same diameter and length at a heating rate of 3 °C/min and corrected to the NIST SRM 736[22] standard profile for Cu in the range of 20–400 °C. Corresponding runs of as-cast MZ1617 and A356.0 were performed with the CTE determined by a linear fit of the data from the range of room temperature to 100 °C.

3. Results and Discussion

3.1 Thermo-Calc Evaluation

The liquidus projection as calculated by Thermo-Calc is shown in Fig. 4a while the isothermal section at 300 °C is shown in Fig. 4b. The solid blue lines on the liquidus projection indicate the lowest temperature liquidus lines, which are typically at the eutectic composition between different phase fields. The desired Al–Mg–Zn alloy compositions, shown by the red dots, indicate hypoeutectic solidification of α-Al and the τ-$Mg_{32}(Al,Zn)_{49}$ phase (henceforth referred to as T-phase) with an equilibrium structure of α + T-phase at 300 °C. Additional simulation by the Scheil solidification method was performed on each alloy to determine the equilibrium and non-equilibrium solidification pathways using the Scheil solidification module in Thermo-Calc. The resulting plots of fraction solid versus temperature is shown in Fig. 5 where the dotted line displays the profile under equilibrium solidification. The equilibrium solidification range is observed to be less than 50 °C for each alloy, which is a characteristic of castable aluminum alloys, while the non-equilibrium solidification paths reveal a much larger solidification range than equilibrium but is the same range for all alloys. Both the equilibrium and non-equilibrium pathways predict the same solidification transformation sequence of

$$Liquid \rightarrow Liquid + FCC\_A1 \rightarrow Liquid + FCC\_A1 + T\_phase \qquad (1)$$

where *FCC_A1* is the α-Al matrix. As the first solid formed, the α-Al phase indicates hypoeutectic solidification for each alloy while T-phase forms from eutectic solidification. Furthermore, Fig. 5 indicates that MZ1617 is predicted to have the largest fraction of primary α-Al formed with nearly 39% α-Al (Fig. 5a) while MZ1920 is predicted to have about 21% primary α-Al (Fig. 5b) and MZ2324 has almost 4% primary α-Al.

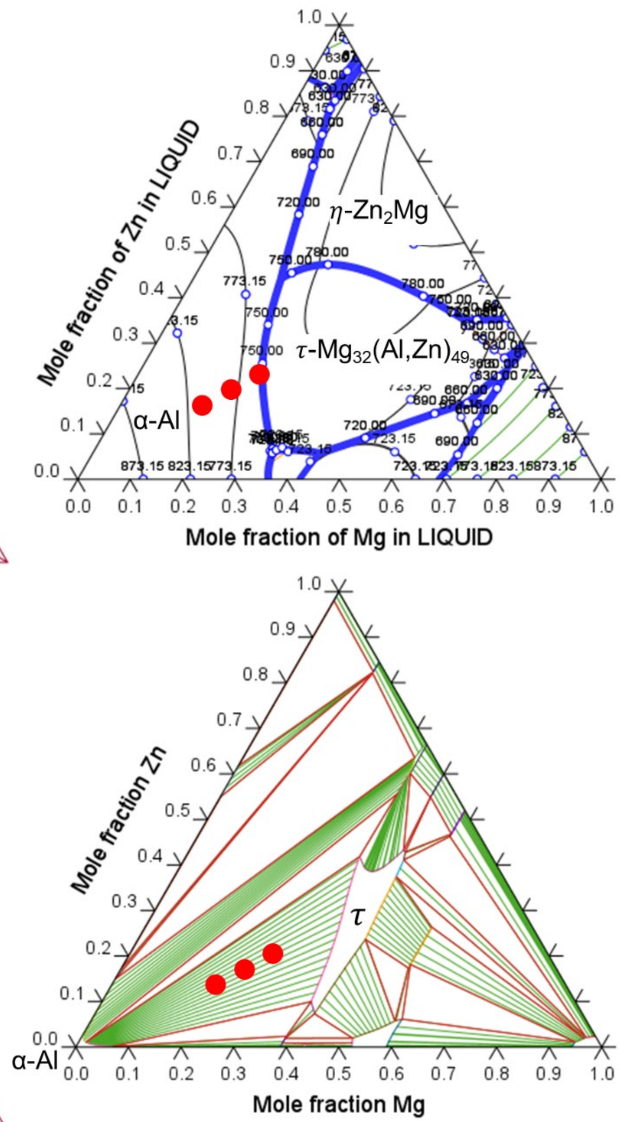

a)

b)

Fig. 4 Thermo-Calc projections of a) liquidus surface and b) isothermal section at 300 °C for the Al–Mg–Zn ternary system with the targeted compositions indicated by the red dots. Isothermal contours of the liquidus projection are given in units of kelvin.

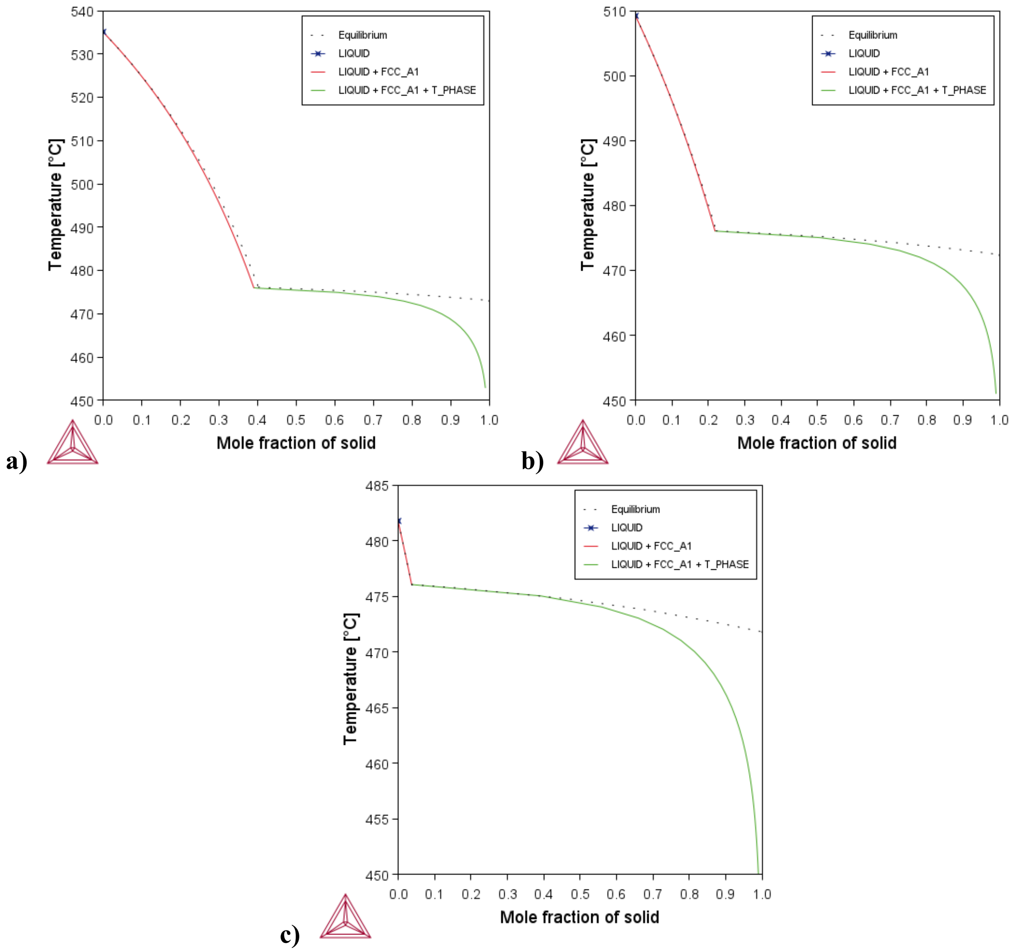

Fig. 5 Scheil solidification pathways for a) MZ1617, b) MZ1920, and c) MZ2324

The composition for each phase as a function of mole fraction solid predicted from Scheil solidification simulation is shown in Fig. 6. For all alloys, the composition of Mg and Zn in primary α-Al is observed to increase with increasing fraction of solid while Al decreases, which suggests that the phase boundaries of primary α-Al will be rich Mg and Zn. The T-phase then precipitates as the composition of the liquid phase becomes enriched in Mg and Zn. As the T-phase fraction increases, the composition of the α-Al phase becomes further enriched in Mg but leaner in Zn as most of the Zn partitions to T-phase. As the T-phase fraction increases, the composition of Mg in T-phase increases while the Zn decreases, indicating the T-phase has a wide range of solubility for Mg and Zn.

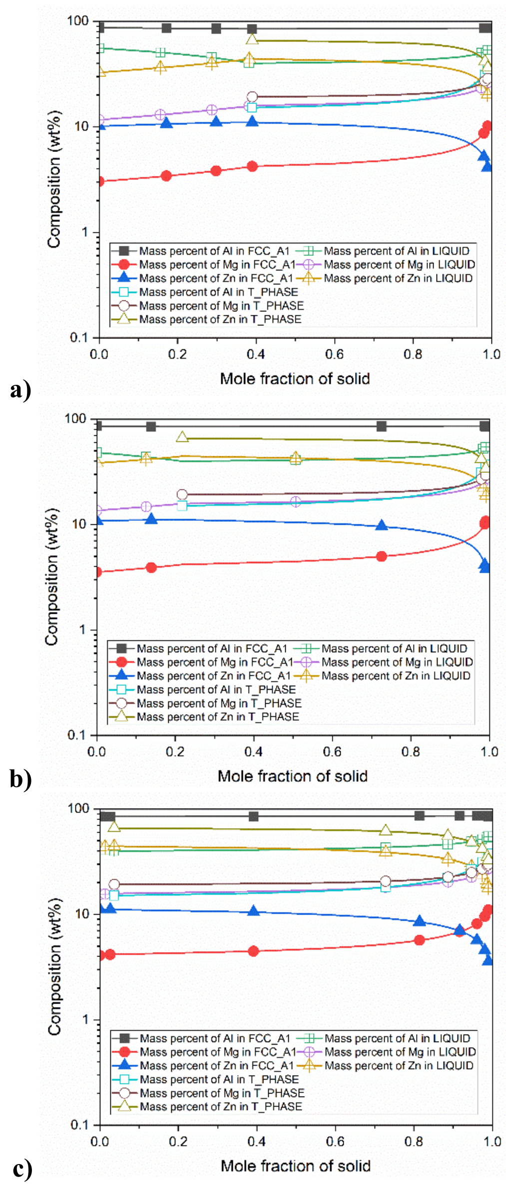

Fig. 6 Composition of phases predicted by Scheil Solidification for a) MZ1617, b) MZ1920, and c) MZ2324

3.2 Characterization of As-Cast Rods

The X-ray diffraction patterns of as-cast rods are shown in Fig. 7. Pattern matching for each alloy revealed only the presence of α-Al and T-phase (PDF 00-019-0029) as was predicted by Thermo-Calc simulations. A characteristic backscattered SEM image of the MZ2324 rod is shown in the top left of Fig. 8a with corresponding EDS map signals for Al (top right), Mg (middle left), and Zn (middle right). The BSE image revealed areas of dark contrast that correspond with the Al EDS signal indicating regions of primary α-Al while the bright contrast areas show a fine, submicrometer cellular eutectic microstructure of α-Al and T-phase where the

T-phase is rich in Mg and Zn (Fig. 8b,c). The boundary between the primary α-Al and cellular dendrite regions show a bright contrast boundary indicating there is enrichment of heavy element (Zn) at the boundary, which agrees with the projections from Scheil solidification.

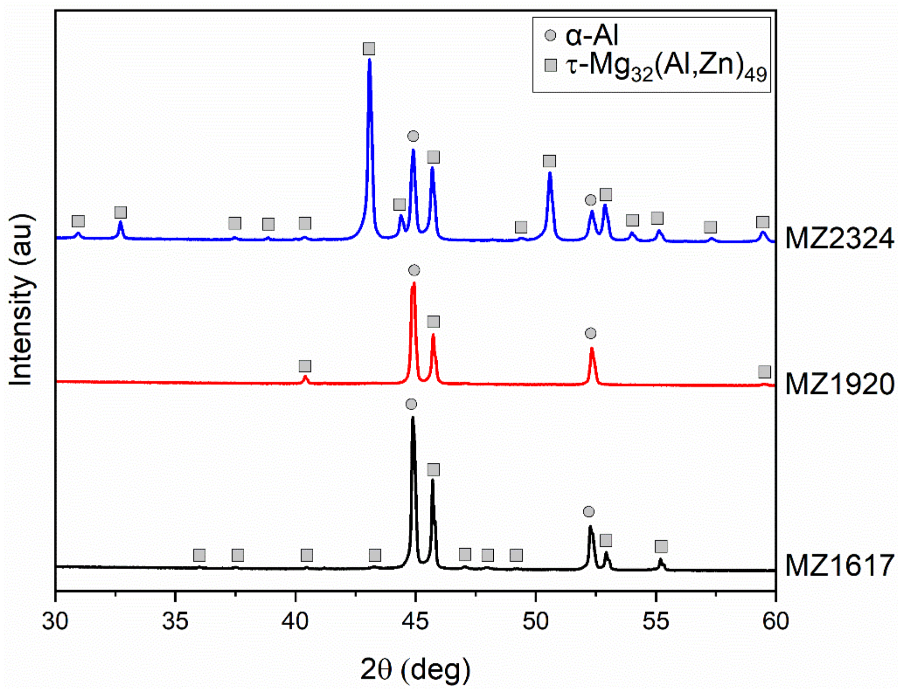

Fig. 7 Powder X-ray diffraction patterns of as-cast rods of each alloy with Co k_α radiation

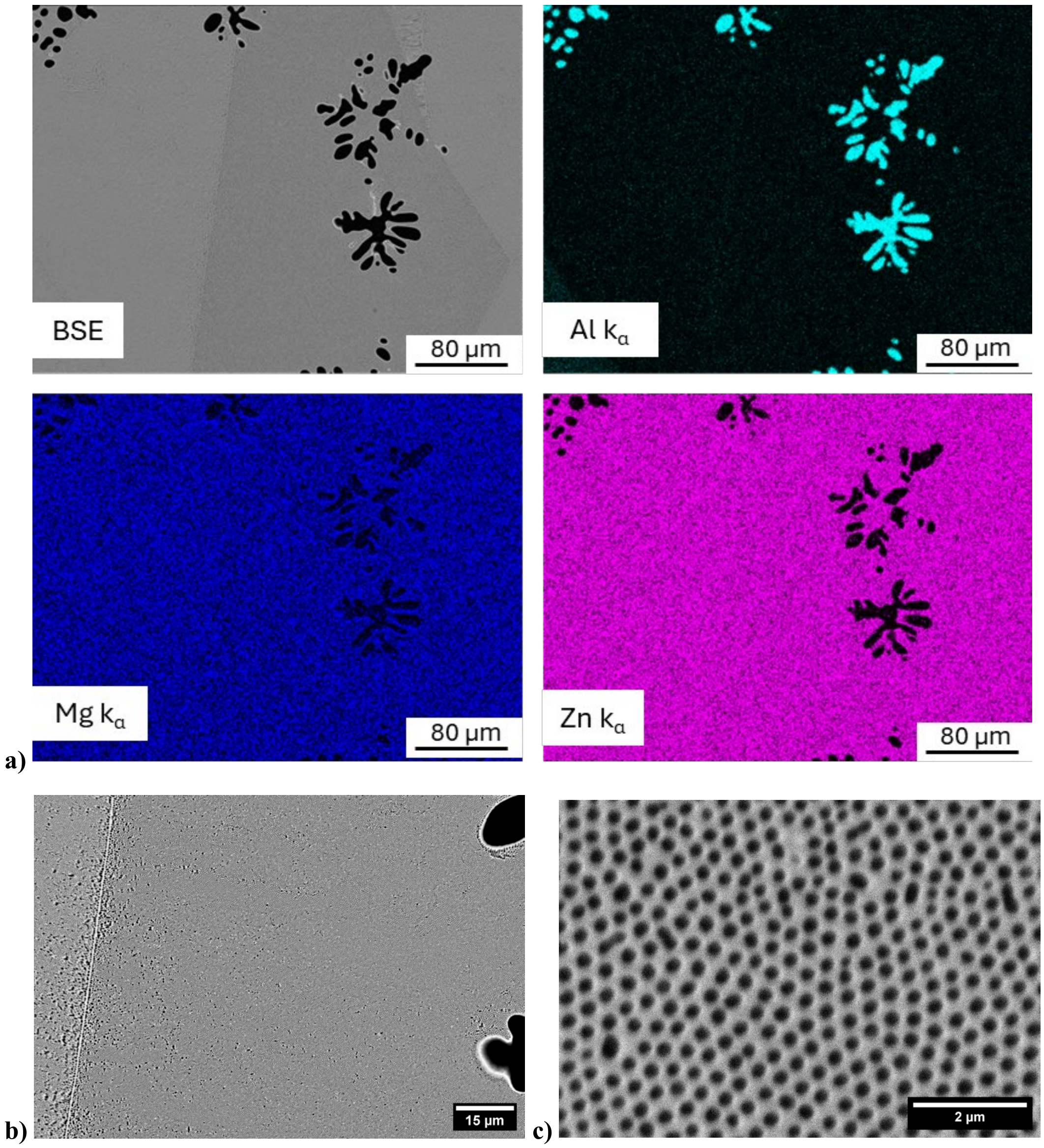

Fig. 8 a) Characteristic backscattered SEM image for the MZ2324 rod with corresponding EDS maps of Al, Mg, and Zn elemental signals. Higher magnification images of the b) primary α-Al and c) cellular eutectic region.

Like MZ2324, MZ1920 (Fig. 9) and MZ1617 (Fig. 10) showed regions of primary α-Al regions with a fine cellular eutectic phase with the area fraction of the α-Al dendrites increasing from MZ2324 < MZ1920 < MZ1617 as expected from Scheil solidification simulations. Indeed, the area fractions of primary α-Al presented in Table 2 are very close to the predictions from the Scheil solidification simulations. Higher magnification images of the α-Al pools (Figs. 9b and 10b) revealed the presence of faint platelets of a medium contrast phase. This is likely T-phase formed from supersaturation of Mg and Zn in the primary α-Al because of non-equilibrium solidification and likely precipitated in solid-state secondary precipitation upon cooling of the cast alloy to room temperature.

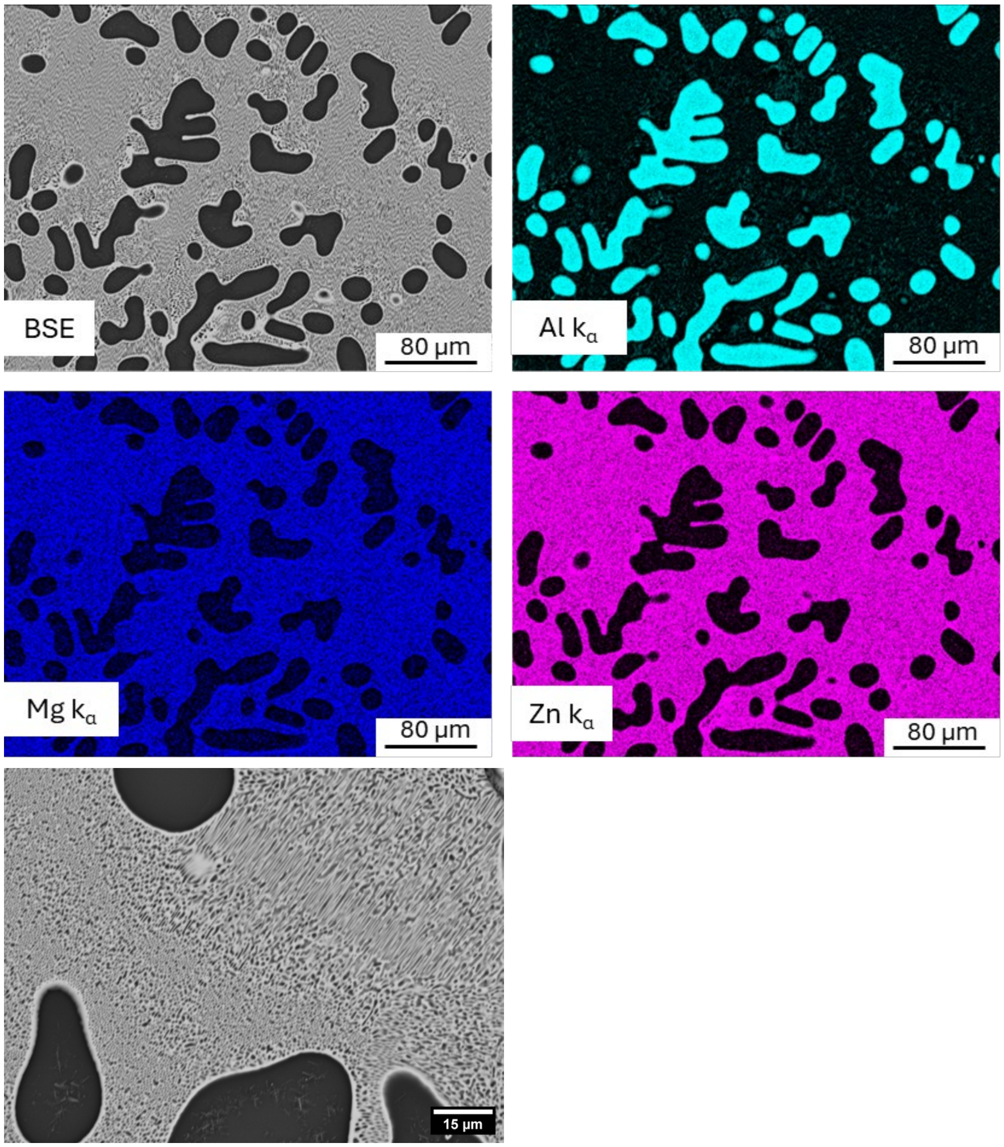

a)
b)

Fig. 9 a) Characteristic backscattered SEM image for MZ1920 with corresponding EDS maps of Al, Mg, and Zn elemental signals. b) Higher magnification backscattered SEM image of the eutectic phase and α-Al dendrite.

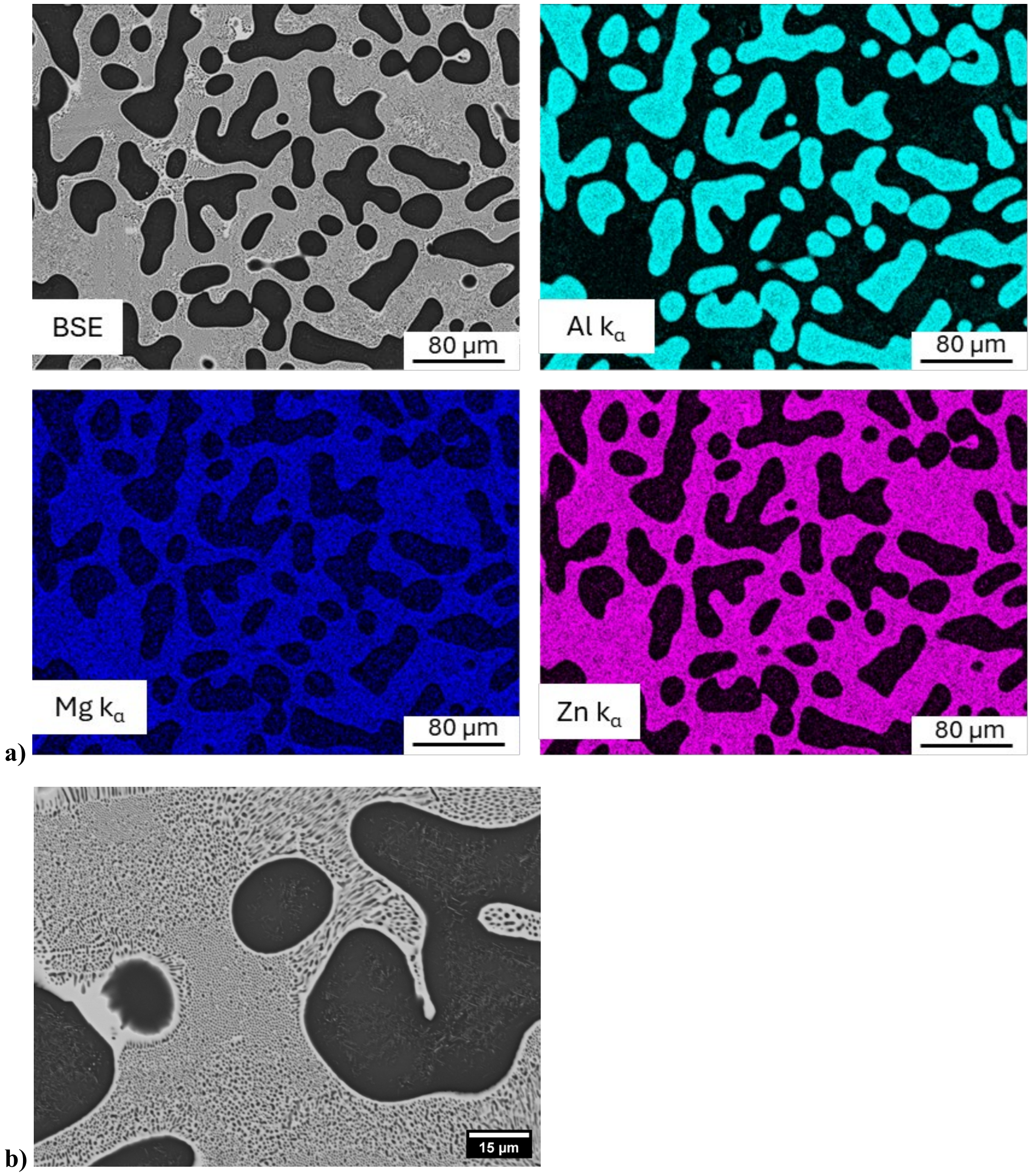

Fig. 10 a) Characteristic backscattered SEM image for MZ1617 with corresponding EDS maps of Al, Mg, and Zn elemental signals. b) Higher magnification backscattered SEM image of the eutectic phase and α-Al dendrite.

Table 2 Area percent hypoeutectic α-Al determined by quantitative image analysis

Alloy	Area fraction primary α-Al
MZ1617	42.5% ± 0.93%
MZ1920	24.2% ± 1.94%
MZ2324	5.76% ± 1.58%

The average measured Vickers microhardness of each alloy rod is given in Table 3. The hardness is observed to increase greatly from MZ1617 < MZ1920 < MZ2324 indicating excellent strengthening increase from T-phase formation and decreasing fraction of primary α-Al. In addition, all alloys displayed a two- to three-times greater hardness than A356.0, indicating the possibility of high-strength alloys. However, observations of the indentation process for each alloy indicated that the MZ alloys are likely very brittle because a cracking of the samples could be heard while the load was applied.

Table 3 Average Vickers microhardness measured on each alloy using a 1-kgf load

Alloy	Average VH_1 (MPa)	Std dev (MPa)
MZ1617	1781	39.9
MZ1920	2117	44.8
MZ2324	2543	94.2
A356.0-T6	876	5.1

3.3 Characterization of Wedge Castings

Attempts were made on each wedge casting to complete the test cut plan outlined in Section 2.3. However, only MZ1617 could be machined by EDM as MZ1920 and MZ2324 were too brittle to be cut without deleterious fracture. Indeed, there were some issues with cutting MZ1617, but samples were machined with success. As such, further tensile and CTE testing were only performed on MZ1617. Optical microscope images of the wedge at different heights from the tip of a vertical center section of the wedge are shown in Fig. 11. The microstructure is observed to be very fine near the tip of the wedge with the primary α-Al phase visible as the lighter contrast phase and the α + T phase eutectic region as the darker contrast. The average size of primary α-Al dendrites increased by nearly an order of magnitude from 3 mm from the tip of the wedge to 68 mm from the tip of the wedge as shown in Fig. 12. In addition, the area fraction of α-dendrites at the 3-mm mark was lower than that of the rest of the wedge indicating a higher fraction of eutectic microstructure. This is likely due to the rapid cooling rate at the tip of the wedge, which kinetically restricts primary phase growth. The high thermodynamic driving force for solidification therefore results in eutectic solidification from the high undercooling. Despite this, the average area fraction of primary α-dendrite of the bulk alloy was similar to that predicted by Scheil solidification in Fig. 5.

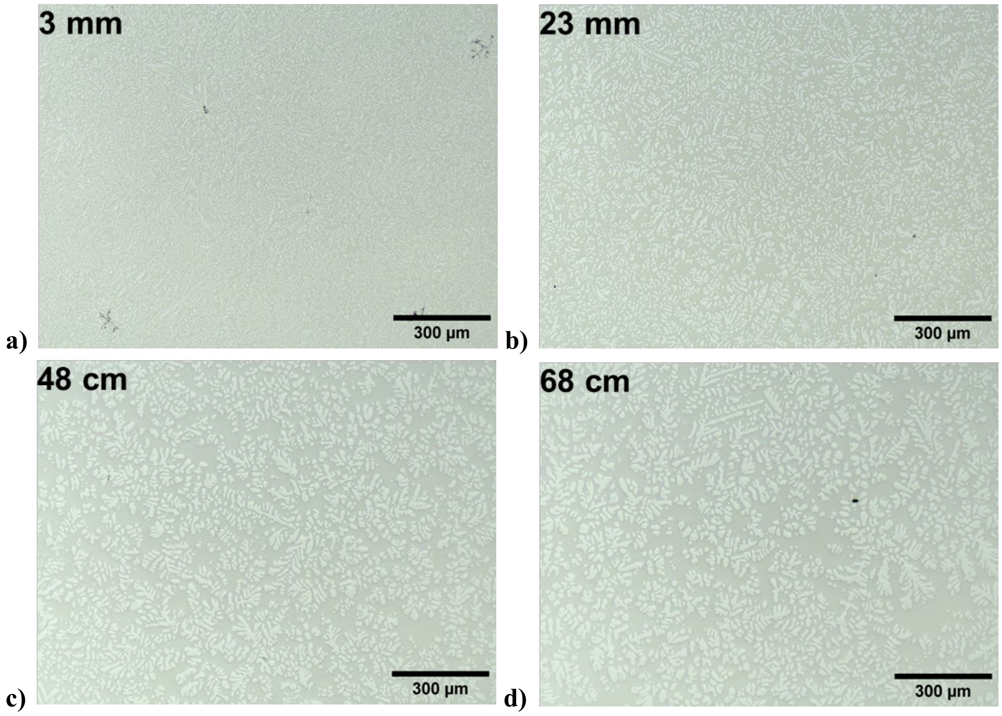

Fig. 11 Optical microscope image of the MZ1617 wedge taken at a) 3 mm, b) 23 mm, c) 48 mm, and d) 68 mm from the tip of the wedge

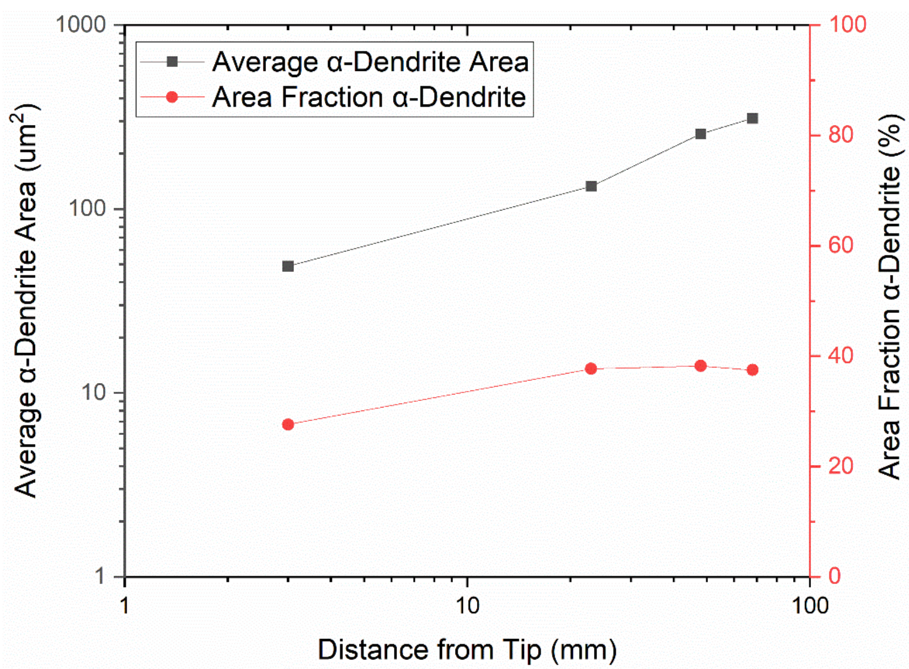

Fig. 12 Average cell size and area fraction of primary α-dendrites as a function of distance from the tip of the cast wedge

The tensile properties of MZ1617 as a function of distance from the tip of the wedge is shown in Fig. 13. The room temperature tensile behavior of MZ1617 did not display any ductility for any of the bars tested; thus, only the fracture strength is reported with a single data point at each distance from the wedge. Assuming that these data points are a valid characterization of the tensile behavior of MZ1617, a small decrease in fracture strength would be observed with increasing distance away from the tip of the wedge. This is not surprising given the changes in the primary α-dendrite size revealed in Fig. 12.

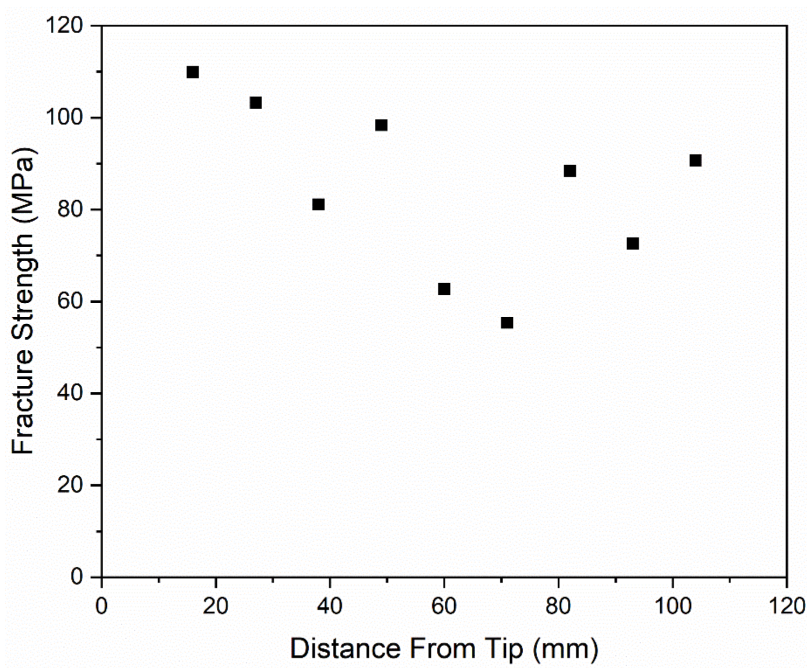

Fig. 13 Tensile fracture strength as a function of distance from the tip of the wedge. Measurements were taken at room temperature.

The results of linear dilatometry experiments for MZ1617 compared to A356.0 are shown in Fig. 14, where the CTE of each alloy can be extracted from the slope of the curves for the plot percent linear change versus temperature. A linear fit of the measured data up to 100 °C provides a basis of comparison to other cast Al alloys whose data beyond 100 °C is scarce. The fit for A356.0 revealed a value of 21.3 µm/m-°C, which is in excellent agreement with the literature value of 21.5 µm/m-°C.[23] The CTE for MZ1617 was measured to be larger than that of A356.0 with a value of 23.7 µm/m-°C up to 100 °C. Furthermore, the difference in CTE increased with increasing temperature, which indicates additional, undesired expansion.

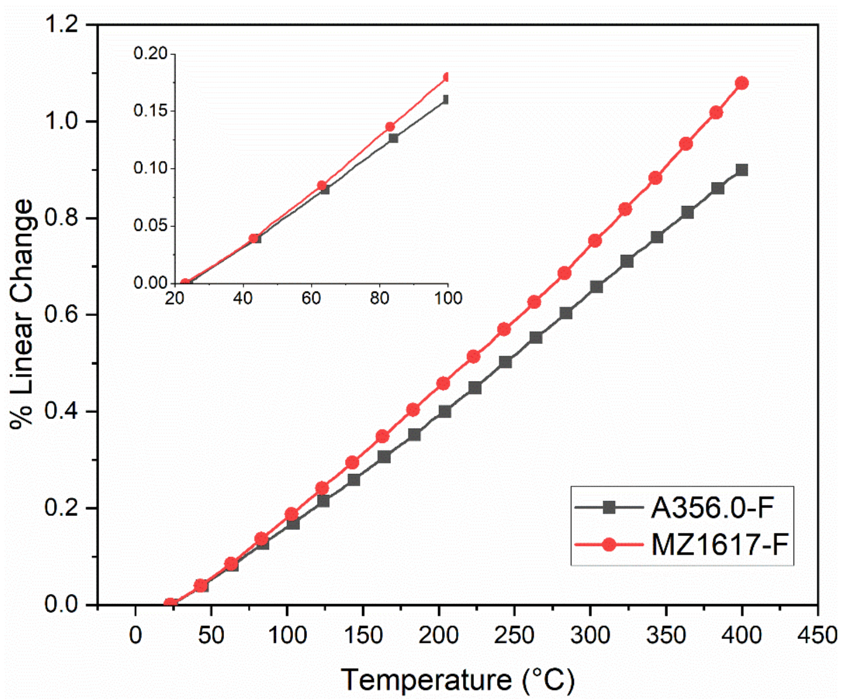

Fig. 14 Dilatometry of MZ1617 and A356.0 in the as-cast condition

4. Conclusions

Three hypoeutectic Al–Mg–Zn alloys were produced via different casting methods. The results indicate that the hardness increases with increasing volume fraction of T-phase due to the high intrinsic hardness of the T-phase. However, practical alloys of the compositions investigated herein were not deemed worthy for industrialization based on negligible room temperature ductility and a high CTE relative to typical aluminum casting alloys.

5. References

1. Sims ZC, Weiss D, McCall SK, McGuire MA, Ott RT, Geer T, Rios O, Turchi PA. Cerium-based, intermetallic-strengthened aluminum casting alloy: high-volume co-product development. JOM. 2016;68(7):1940–1947.

2. Plotkowski A, Rios O, Niyanth FS, Sims ZC, Unocic KA, Ott R, Dehoff RR, Babu S. Evaluation of an Al–Ce alloy for laser additive manufacturing. Acta Materialia. 2017;126:507–519.

3. Stromme ET, Henderson HB, Sims Z, Kesler MS, Weiss D, Ott R, Meng F, Kassoumeh S, Evangelista J, Begley G, et al. Ageless aluminum-cerium-based alloys in high-volume die casting for improved energy efficiency. JOM. 2018;70(6):866–871.

4. Czerwinski F. Critical assessment 36: assessing differences between the use of cerium and scandium in aluminium alloying. J Mater Sci Technol. 2020;36(3):255–263.

5. Medvedev AE, Murashkin MY, Enikeev NA, Bikmukhametov I, Valiev RZ, Hodgson PD, Lapovok R. Effect of the eutectic Al-(Ce,La) phase morphology on microstructure, mechanical properties, electrical conductivity and heat resistance of Al-4.5(Ce,La) alloy after SPD and subsequent annealing. J Alloys Compd. 2019;796:321–330.

6. Weiss D. Improved high-temperature aluminum alloys containing cerium. J Mater Eng Perform. 2019;28(4):1903–1908.

7. Akopyan TK, Belov NA, Naumova EA, Letyagin NV, Sviridova TA. Al-matrix composite based on Al-Ca-Ni-La system additionally reinforced by L1 type nanoparticles. Trans Nonferrous Met Soc China. 2020;30(4):850–862.

8. Ng DS, Dunand DC. Aging- and creep-resistance of a cast hypoeutectic Al-6.9Ce-9.3Mg (wt.%) alloy. Mater Sci Eng A. 2020;786:139398.

9. Ajantiwalay T, Michi R, Roach C, Shyam A, Plotkowski A, Devaraj A. Influence of microstructural heterogeneities on small-scale mechanical properties of an additively manufactured Al–Ce–Ni–Mn alloy. Addit Manuf Lett. 2022;3.

10. Kozakevich J. Stroh J, Mallouhi V, Sediako D, Weiss D. Interplay between cooling rate, microstructure, and mechanical properties of an Al–Ce–Ni–Mn alloy. Light Met. 2022:83–91.

11. Michi RA, Sisco K, Bahl S, Yang Y, Poplawsky JD, Allard LF, Dehoff RR, Plotkowski A, Shyam A. A creep-resistant additively manufactured Al–Ce–Ni–Mn alloy. Acta Materialia. 2022;227:117699.

12. Wu T, Plotkowski A, Shyam A, Dunand DC. Microstructure and creep properties of cast near-eutectic Al–Ce–Ni alloys. Mater Sci Eng A. 2022;833:142551.

13. Emery R, Rios OR, Lass EA, Jorgensen CS, Gilbert DA, Meier WR, Koehler MR, Rack PD. Identification of low coefficient of thermal expansion in Al23Ce4Ni6 via combinatorial sputtering of Al–Ce–Ni–Mn thin films and upscaling to bulk materials. J Alloys Compd. 2023;968:172220.

14. Kozakevich JR, Stroh J, Sediako D, Weiss D. Solidification kinetics of an Al–Ce alloy with additions of Ni and Mn. Metals. 2023;13(5).

15. Michi RA, Simpson JJ, Bahl S, Campbell Q, Brackman P, Plotkowski A, Dehoff RR, Haynes JA, Wang Q, Shyam A. Additively manufactured Al–Ce–Ni–Mn alloy with improved elevated-temperature fatigue resistance. Addit Manuf. 2023;66:103477.

16. Perrin AE, Michi RA, Leonard DN, Sisco KD, Plotkowski AJ, Shyam A, Poplawsky JD, Allard LF Jr, Yang Y. Effect of Mn on eutectic phase equilibria in Al-rich Al–Ce–Ni alloys. J Alloys Compd. 2023;965:171455.

17. Sisco KD, Plotkowski A, Yang Y, Allard L, Fancher C, Rawn C, Poplawsky JD, Dehoff R, Babu SS. Heterogeneous phase transformation pathways in additively manufactured Al–Ce–Mn alloys. J Alloys Compd. 2023;938:168490.

18. Takata N, Okano T, Aikawa M, Suzuki A, Kobashi M, Hagihara K. Morphology and mechanical properties of the T-Al6Mg11Zn11 phase in the eutectic microstructure of Al–Zn–Mg ternary alloys. Intermetallics. 2020;124:106881.

19. Anderson K, Weritz J, Kaufman JG, editors. Properties and selection of aluminum alloys. ASM International; 2019.

20. Cain T, Mogonye J-E. Method for laboratory-scale wedge casting of aluminum alloys. DEVCOM Army Research Laboratory (US); 2021 Nov. Report No: ARL-TN-1092.

21. ASTM E8. Standard test methods for metal tensile testing. ASTM International; 2024 May 20.

22. NIST SRM 734. Thermal conductivity of electrolytic iron. National Institute of Standards and Technology; 1975 Mar 5.

23. 356.0 and A356.0[1]: Al–Si–Mg high-strength casting alloys. In: Anderson K, Weritz J, Kaufman JG, editors. Properties and selection of aluminum alloys, vol 2B. ASM International; 2019.

List of Symbols, Abbreviations, and Acronyms

Al	aluminum
Al_2O_3	aluminum oxide
Ar	argon
ARL	Army Research Laboratory
ASTM	American Society for Testing and Materials
BSE	backscatter electron
CAMI	Coated Abrasives Manufacturing Institute
Ce	cerium
Co	cobalt
CTE	coefficient of thermal expansion
Cu	copper
DEVCOM	US Army Combat Capabilities Development Command
EDM	electrical discharge machining
EDS	energy-dispersive X-ray spectroscopy
ID	identification
kgf	kilogram force
Mg	magnesium
SEM	scanning electron microscopy
SiC	silicon carbide
Std dev	standard deviation
VH	Vickers microhardness
Zn	zinc

1 (PDF)	DEFENSE TECHNICAL INFORMATION CTR DTIC OCA
1 (PDF)	DEVCOM ARL FCDD RLB CI TECH LIB